THE JOURNAL OF PHYSICAL CHEMISTRY C

Article

Cite This: J. Phys. Chem. C 2018, 122, 17423−17436

pubs.acs.org/JPCC

Experimental TDPAC and Theoretical DFT Study of Structural, Electronic, and Hyperfine Properties in (^{111}In →)^{111}Cd-Doped SnO_2 Semiconductor: *Ab Initio* Modeling of the Electron-Capture-Decay After-Effects Phenomenon

Germán N. Darriba,*[,†] Emiliano L. Muñoz,[‡] Artur W. Carbonari,[§] and Mario Rentería*[,†]

[†]Departamento de Física and Instituto de Física La Plata (IFLP, CONICET-UNLP), Facultad de Ciencias Exactas, Universidad Nacional de La Plata, CC 67, 1900 La Plata, Argentina

[‡]Facultad de Ingeniería, Universidad Nacional de La Plata, 1900 La Plata, Argentina

[§]Instituto de Pesquisas Energéticas e Nucleares-IPEN/CNEN, Universidade de São Paulo, São Paulo, SP, Brazil

ABSTRACT: In this paper we investigate the effect of Cd doping at ultralow concentrations in SnO_2 both experimentally, by measuring the temperature dependence of the electric quadrupole hyperfine interactions with time-differential $\gamma-\gamma$ perturbed angular correlation (TDPAC) spectroscopy using ^{111}Cd as probe nuclei, and theoretically, by performing first-principles calculations based on the density functional theory. TDPAC spectra were successfully analyzed with a time-dependent *on−off* model for the perturbation factor. These results show combined dynamic plus static interactions whose electric-field-gradients were associated in this model to different stable electronic configurations close to the Cd atoms. The dynamic regime is then originated in fast fluctuations between these different electronic configurations. First-principles calculation results show that the Cd impurity introduces a double acceptor level in the top of the valence band of the doped semiconductor and produces isotropic outward relaxations of the nearest oxygen neighbors. The variation of the calculated electric-field gradient tensor as a function of the charge state of the Cd impurity level shows an interesting behavior that explains the experimental results, giving strong support from first-principles to the *electron-capture after-effects* proposed scenario. The electron-capture decay of the parent ^{111}In to ^{111}Cd as well as the double acceptor character of the ^{111}Cd impurity and the electric nature of the host are shown to contribute to the existence of these types of time-dependent hyperfine interactions.

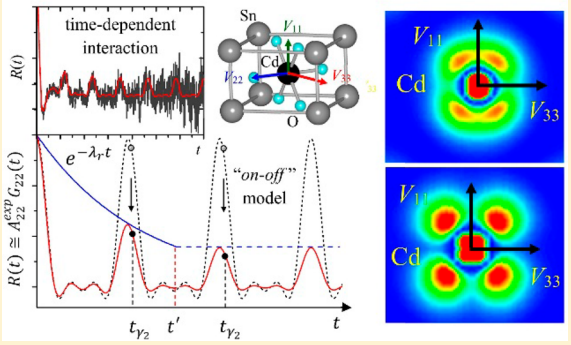

I. INTRODUCTION

The wide-bandgap SnO_2 semiconductor is a very attractive material for a wide variety of technological applications, due to its electrical and optical properties as well as its thermal and chemical stability. It has been used in the construction of solar cells,[1] flat panel collectors, touch panels,[2] and sensors for gas detection.[3,4] It is well-known that the inclusion of certain impurities in SnO_2 can improve these properties.[5−8] More recently, Cd has been revealed as an ideal dopant for some of these properties. For example, in the case of gas sensors, the Cd doping (i.e., the Sn^{4+} substitution by Cd^{2+}) induces the formation of oxygen vacancies, enhancing the sensor performance with respect to undoped n-type SnO_2 (in which natural oxygen vacancies may be present in the real samples) at the same operating temperature.[9] On the other hand, the inclusion of Cd impurities in SnO_2 nanoparticles has revealed a dielectric constant loss behavior at high frequencies[10] suggesting its application in many electronic devices. Concerning optoelectronic applications, Mariappan et al.[11] developed Cd-doped SnO_2 thin films, enhancing their electrical conductivity and optical transmittance when 5% of Cd doping was used.

In the last years, in condensed-matter physics, structural, electronic, and magnetic properties in pure and doped systems have been carefully studied at the atomic scale confronting results from hyperfine experimental techniques with reliable all-electron (AE) *ab initio* predictions in the framework of the density functional theory (DFT).[12−20] In particular, the subnanoscopic environment of impurities or native atoms in solids can be studied employing the time-differential perturbed $\gamma-\gamma$ angular-correlation (TDPAC) spectroscopy. This technique provides a very precise characterization of the electric-field-gradient (EFG) tensor at diluted (ppm) radioactive probe atoms. The EFG is a symmetric tensor of second-order with components defined by $V_{ij}(\vec{r}) = \frac{\partial^2 V(\vec{r})}{\partial x_i \partial x_j}$. Here, $V(\vec{r})$ is the electric potential generated by the charge density nearby a probe nucleus. Particularly, the EFG tensor is diagonal in the principal axis system and may be characterized by only its

Received: April 19, 2018
Revised: June 13, 2018
Published: July 3, 2018

DOI: 10.1021/acs.jpcc.8b03724
J. Phys. Chem. C 2018, 122, 17423−17436

largest component V_{33} and the asymmetry parameter defined as $\eta = (V_{11} - V_{22})/V_{33}$, with $0 \le \eta \le 1$ using the $|V_{11}| \le |V_{22}| \le |V_{33}|$ standard convention. In summary, from the determination of the EFG tensor it is possible to obtain very valuable information about the impurity−host system under study, such as structural distortions, localization of impurities and defects, as well as their charge state, etc., and this information could be obtained by confrontation of the experimental results with accurate theoretical predictions of the EFG.

As it is well-known, the (^{111}In →)^{111}Cd and (^{181}Hf →)^{181}Ta nuclides are the most used probe atoms in TDPAC spectroscopy, both as a native atom or as an impurity in a given system. In the case of (^{181}Hf →)^{181}Ta-doped SnO_2, many experimental TDPAC studies have been reported in different kinds of samples and annealing conditions (SnO_2 and Sn−O thin films,[21,22] sol−gel-prepared nanopowders[23]). Particularly, a complete study combining TDPAC experiments on ^{181}Hf-(→^{181}Ta)-implanted SnO_2 thin films and *ab initio* calculations in Ta-diluted SnO_2 has been performed in detail.[15] This double approach enabled us to determine the structural relaxations introduced in the host, the correct charge state of the impurity, and the metallic behavior of a degenerate semiconductor (in agreement with resistivity experimental results obtained in samples with the same Ta dilution), and we could understand the origin of the EFG invariance with temperature observed in the TDPAC measurements.

On the other hand, for the (^{111}In →)^{111}Cd-doped SnO_2 system, the existing TDPAC experiments reported in the literature[23−28] are not conclusive with respect to the interpretation of the hyperfine parameters reported, and their temperature dependence remains controversial. Besides the sample preparation and their activation, one of the difficulties in the analysis of these TDPAC spectra resides in the fact that the transmutation of ^{111}In to ^{111}Cd is produced by nuclear electron capture (EC) (^{111}In(EC) → ^{111}Cd), giving rise to the electronic relaxation process usually called in the literature (electron-capture-decay) "after-effects" (ECAE).[29−31]

The first TDPAC results of ^{111}Cd-doped SnO_2 were reported by Wolf et al.[24] In their experiments, the ^{111}In(→^{111}Cd) probe's parent was diffused into SnO_2 powder samples and measured in the temperature (T) range 4−1260 K. They found a unique hyperfine interaction (characterized by ω_Q = 18.2(1) Mrad/s and η = 0.1(1), temperature independent), split into a *static* and a *dynamic* part. They found a temperature dependence of the fraction (f) of probes that senses the static part of this interaction, varying from 25% at T = 4 K to 70% at T > 1000 K. They attributed this dependence to the ECAE and to the fact that the perturbation depends on the local electronic density and proposed the generation of unfilled inner electron shells to explain this temperature dependence. Giving support to these ideas, they observed a faster increase of f as T increases when the SnO_2 samples were doped with "donor" H_2 atoms. The presence of a unique hyperfine interaction was consistent with the single nonequivalent Sn site of the rutile structure. Bibiloni et al.[25] performed TDPAC experiments diffusing ^{111}In(→^{111}Cd) atoms into pure Sn foils (and then oxidizing the activated samples to obtain ^{111}In-doped SnO_2) and in high purity SnO_2 powders. For both kinds of samples two static hyperfine interactions were observed (characterized at room temperature (RT) by ω_{Q_1} = 31.1(9) Mrad/s, η_1 = 0.45(4) and ω_{Q_2} = 14.3(6) Mrad/s, η_2 = 0.65), with their populations varying as a function of T in the 17−1173 K range. These interactions were assigned to ^{111}Cd probe atoms located at substitutional Sn sites with singly and doubly ionized oxygen vacancies as near neighbors, respectively. Subsequently, similar hyperfine interactions governed by the same temperature dependence were observed by Moreno et al.[26] diffusing ^{111}In(→^{111}Cd) probes into SnO_2 thin films (employing two different backing substrates). Bibiloni et al.[25] and Moreno et al.[26] did not find in their investigations any evidence of the existence of a time-dependent interaction arising from the ECAE. Finally, Rentería et al.[27] performed TDPAC experiments at RT in air on ^{111}In(→^{111}Cd)-implanted Sn−O films after each step of thermal annealings up to 1023 K. Initially, they found two coexistent phases, disorder SnO and SnO_2, which were transformed by an appropriate annealing treatment into the SnO_2 crystalline phase. Four hyperfine interactions were needed to reproduce the TDPAC spectra, two corresponding to ^{111}Cd in SnO and the other two to ^{111}Cd in SnO_2. The hyperfine parameters of ^{111}Cd in the crystalline SnO_2 phase were ω_Q = 18.4(1) Mrad/s and η = 0.18(2), in agreement with the hyperfine parameters found by Wolf et al.,[24] but without evidence of a time-dependent interaction. It should be mentioned that this EFG is also in agreement with one of the hyperfine interactions observed by Bibiloni et al.,[25] which was only observed at T = 1073 K. In addition, one of the two static hyperfine interactions observed in ^{111}In-doped sol−gel-prepared SnO_2 nanopowders,[23,28] characterized by $\omega_Q \sim 18$ Mrad/s and $\eta \sim 0.1$ in the temperature range 77−1000 K, is also in agreement with that reported by Wolf et al.[24] On the other hand, one of the two static hyperfine interactions observed in ^{111}In-implanted SnO_2 thin films,[23] assigned to probes at substitutional cation sites, is characterized by a mean value $\omega_Q \sim 16.5$ Mrad/s in the 293−923 K temperature range. The ω_Q values of the relevant hyperfine interactions assigned to ^{111}Cd probes localized at substitutional Sn sites in crystalline SnO_2, prepared and doped by different methods and reported in the above-mentioned previous experiments, are condensed in Figure 1.

Taking into account all of these previous and dissimilar experimental results and their interpretations and in order to solve this controversy, we performed new and careful TDPAC experiments in high purity SnO_2 polycrystalline samples. With the aim to maximize the percentage of ^{111}Cd probes located in defect-free Sn sites, we diffused ^{111}In(→^{111}Cd) into SnO_2 powders under a nonoxidant N_2 atmosphere. The TDPAC measurements were carried out as a function of temperature, in order to study the ECAE phenomenon. In addition, we performed a complete *ab initio*/DFT study that gives a reliable description of structural and electronic effects introduced by the impurity in this semiconductor oxide, without the use of external parameters and self-consistently. We performed this detailed study as a function of the charge state of the impurity, which enables us to present an *ab initio* scenario to interpret the ECAE phenomenon.

In what follows, we present the TDPAC technique, the data reduction, the sample preparation, and the time-dependent perturbation factor used to analyze the experimental results, which are shown in Section II. In Section III we present the first-principles procedure and discuss the corresponding theoretical predictions for the EFG and for the electronic and structural properties of Cd-doped SnO_2. In Section IV we discuss the experimental and the *ab initio* results, presenting an

DOI: 10.1021/acs.jpcc.8b03724
J. Phys. Chem. C 2018, 122, 17423−17436

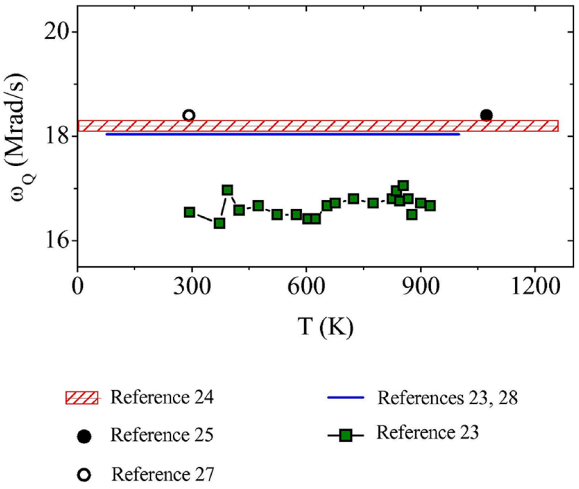

Figure 1. Experimental nuclear quadrupole frequencies (ω_Q) reported in the literature, assigned to (^{111}In →)^{111}Cd localized at substitutional Sn sites in the rutile SnO_2 crystalline phase, determined in TDPAC experiments using ^{111}In-diffused SnO_2 powders (red slashed region); ^{111}In-diffused in Sn foils with subsequent oxidation (black solid circle) and ^{111}In-implanted Sn−O thin films with subsequent annealings up to the rutile crystalline phase (black open circle); ^{111}In-diffused during sol−gel preparation of SnO_2 nanopowders (blue line); and ^{111}In-implanted SnO_2 thin films (green squares). The asymmetry parameter of all these interactions is ∼0.1.

ab initio model for the ECAE, and finally, in Section V we present our conclusions.

II. EXPERIMENTAL SECTION

II.A. TDPAC Spectroscopy, Data Reduction, and Time-Dependent Perturbation Factor. TDPAC spectroscopy is based on the conservation of the angular momentum, and basically it consists of the determination of the perturbation (generated by extranuclear fields) on the correlation between the emission directions of two successive γ radiations (γ_1 and γ_2) during a nuclear decay. This perturbation occurs during the lifetime of the intermediate state of the γ_1−γ_2 cascade. For a complete description of this spectroscopy, see refs 32−34.

In a TDPAC experiment we measure the number of coincidences $C(\Theta,t)$ between γ_1 and γ_2 photons detected at two relative angular positions of the scintillators, $\Theta = 90°$ and $\Theta = 180°$, with t being the elapsed time between both emissions. Hence, the experimental spin-rotation curve or $R(t)$ TDPAC spectrum can be constructed as[35]

$$R(t) = 2\frac{C(180°) - C(90°)}{C(180°) + 2C(90°)} \cong A_{22}^{exp} G_{22}^{exp}(t) \quad (1)$$

where A_{22}^{exp} is the experimental anisotropy of the γ_1−γ_2 cascade and $G_{22}^{exp}(t)$ is the theoretical perturbation factor $G_{22}(t)$ folded with the time−resolution curve of the spectrometer.

The TDPAC experiments presented here were performed using the 171−245 keV γ−γ cascade of ^{111}Cd, produced after the EC nuclear decay of the parent ^{111}In nuclide.

In what follows we will show the construction and justification of the perturbation factor used to describe the time-dependent hyperfine interactions observed in the TDPAC experiments reported in the present work. This analytic perturbation factor was proposed by Bäverstam et al.[36] (BO) and is a modification of that proposed by Abragam and Pound (AP) used to describe the randomly fluctuating dynamic (i.e., time-dependent) hyperfine interaction sensed by a probe-nucleus in a liquid environment.[37] In the BO model, a modification was introduced in order to account for the *on*−*off* character of the dynamic hyperfine interaction, a character that is related to the probe-atom probability to decay to a certain stable electronic ground state (turning *off* the dynamic interaction), during the time window of the TDPAC measurement, leading to a final static interaction.

The type of dynamic interaction we want to describe here is originated in the radioactive decay of the parent of the TDPAC probe if this decay leaves the probe atom in a highly ionized state far from the equilibrium. This occurs, e.g., in the K-electron-capture decay of ^{111}In to ^{111}Cd, the probe used in this work. This process produces an electronic hole in the K shell of the Cd atom, which is filled up with an electron of the outer shells too fast to have any influence on the TDPAC spectra. After this, and due to subsequent Auger processes, the probe ion loses a large number of electrons, leaving the corresponding number of electronic holes, which will diffuse toward the outer atomic shells in less than 10^{-12} s. This first part of the atomic recovery is independent of the environment of the probe atom and again does not influence the TDPAC spectra. However, the following phase during which the outer holes are filled up depends on the probe surroundings. In a solid, the highly ionized charge state of the Cd probe atom becomes almost compensated by electrons from their neighboring ions in a very short time ($\approx 10^{-12}$ s). In the electronic band structure description of the solid, these holes diffuse along the valence band very fast. This happens before the emission of the first γ-ray of the γ_1−γ_2 cascade through which the ^{111}Cd nucleus decays to its (nuclear) ground state (the emission of γ_1 starts the TDPAC measurement, and that of γ_2 ends it).

Only ions with very few *extra* electronic holes with respect to those nominally introduced by a neutral Cd atom substituting a host cation (in our case, i.e., Cd-doped SnO_2, two holes are nominally produced) may live for times long enough (longer than 10^{-12} s) to reach the sensitive time window of the measurement. The necessary condition for this phenomenon to take place seems to be that the probe atom should be embedded in an insulating or semiconducting environment.[24,29,38−44] During the time window of the measurement, transitions among all the resulting potential probe's charge states (including a final stable charge state) can occur, and the probe nucleus will feel fluctuating EFGs due to the transitions among different electronic configurations of the probe atom and its nearest neighbors.

Differently from other proposals that lead to numerical simulations of the $R(t)$ spectrum (see, e.g., ref 45), one of the advantages of the BO model is that it leads to an analytical expression for the perturbation factor that can be used for the spectra fitting. In the last years, this model has been used to analyze time-dependent hyperfine interactions in TDPAC experiments using ^{111}In as a probe atom in oxides[46,47] and, very recently, in pure semiconductors.[48] We describe now in more detail the construction of the perturbation factor in the BO[45] model used to analyze the TDPAC results in this work.[45]

The most general expression for the perturbation factor $G_{kk}(t)$ may be written as[36]

$$G_{kk}(t) = \sum_i c_i e^{a_i t} \quad (2)$$

where c_i and a_i may be complex numbers.

DOI: 10.1021/acs.jpcc.8b03724
J. Phys. Chem. C 2018, 122, 17423−17436

In the case of *static* (time-independent) electric−quadrupole interactions, i.e., when the electronic environment of the probe nucleus does not change during the time interval defined by the emission of γ_1 and γ_2, the perturbation factor, $G_{22}^{s}(t)$, for nuclear−electric−quadrupole interactions, polycrystalline samples, and spin $I = 5/2^+$ of the intermediate nuclear level of the $\gamma_1-\gamma_2$ cascade (as in the case of ^{111}Cd) is[35]

$$G_{22}^{s}(t) = S_{20} + \sum_{n=1}^{3} S_{2n}(\eta)\cos(\omega_n(\eta)t)e^{-\delta\omega_n t} \tag{3}$$

where the coefficients S_{2n} and the interaction frequencies ω_n are known functions[49] of the asymmetry parameter η, ω_n being proportional to the nuclear quadrupole interaction frequency $\omega_Q = eQV_{33}/40\hbar$.[35] In eq 3, we used $k = 2$ since A_{44} is very small for this $\gamma-\gamma$ cascade.

In the case that the following conditions are satisfied (as may be the case of randomly fast fluctuating electronic environments sensed by the TDPAC probe):

(i) the correlation time τ_c, which is a typical time for the changes of the nuclear environments that will originate a time-dependent interaction, is small enough to let $\omega_Q \ll 1/\tau_c$;
(ii) the time of observation t $\gg \tau_c$;
(iii) the fluctuating interaction is so small that the first-order perturbation theory is valid.

Then a *pure dynamic* (i.e., time-dependent) perturbation factor is obtained as[36,37]

$$G_{22}^{dyn}(t) = e^{-t/\tau_r} = e^{-\lambda_r t} \tag{4}$$

and τ_r (= $1/\lambda_r$) is called the relaxation time constant. In our case atomic recombination and electronic de-excitation time constants are included in τ_r. These processes have very short correlation times τ_c. Thus, conditions (i) and (ii) seem to be fulfilled. In our case, as also occurred in ref 36, it is sufficient to fit the $R(t)$ spectra with only one exponential as in eq 4, showing that the fluctuating interaction is small. On other hand, if the fluctuating interaction is stronger than what is assumed in (iii), $G_{22}^{dyn}(t)$ will be the sum of two exponentials, according to the Dillenburg and Maris theory.[50]

The shape of the TDPAC spectra in our experiments (yet observed in many TDPAC experiments in semiconducting and insulating oxides using ^{111}In; see refs 29−31, 46, and 51) suggests that the nuclei of the excited ^{111}Cd atoms are feeling a static electric-field gradient (namely, that corresponding to a certain ^{111}Cd final electronic stable state) besides a dynamic hyperfine interaction (represented by the exponential factor of eq 4). Since, in addition, the static interaction is much weaker than the dynamic one (i.e., the exponential decay is strong, this can be seen in the fast damping of the spectra), $G_{22}(t)$ can be well described, for the *combined* static and dynamic interactions, as the product[36,45]

$$G_{22}(t) = G_{22}^{s}(t)e^{-\lambda_r t} \tag{5}$$

This equation represents a static perturbation factor with a time-dependent anisotropy which decreases to zero for very large times. This is not exactly the shape of our $R(t)$ spectra, which remains undampened after a certain time t. The fact that the excited atoms after a certain time will reach their final stable electronic states (these states may be different at each temperature and not necessarily *the* ground state at each temperature), i.e., the turning *off* of the dynamic interaction, had not yet been accounted for in eq 5. To do this, two simplifying assumptions were made:

(i) That the probability for an atom (per unit time) reaching its final stable electronic state at time t' (measured from the emission time of γ_1) is[36]

$$P_g(t') = \lambda_g N e^{-\lambda_g t'} \tag{6}$$

where N is the number of probes that will contribute to $G_{22}(t)$ at time t (those probes that emit γ_2 at time t), and λ_g is the probability per unit time for an atom to reach this final stable electronic state.

(ii) That the mean (dynamic) interaction strength averaged over all excited atoms is constant, i.e., λ_r is still a constant.

After the N atoms reach their final stable electronic state (at a time t', different for each atom), the hyperfine interaction they produce becomes static. In principle, each atom can reach its final stable electronic state as a continuous relaxation process, but in the BO model no time distribution around t' is taken into account (i.e., the *on−off* electronic transition for each atom is consider "sharp" and occurs instantaneously at a certain t'). Thus, $G_{22}(t)$ may now be seen as an average of the perturbation factors affecting the N probe nuclei. The contribution to the perturbation factor, at time t, corresponding to a probe that arrives at the final stable electronic state at time t', is (remember that γ_2 is emitted at time t):[45]

$$G_{22}(t, t') = \begin{cases} G_{22}^{s}(t)e^{-\lambda_r t'} & \text{if } t > t' \\ G_{22}^{s}(t)e^{-\lambda_r t} & \text{if } t < t' \end{cases} \tag{7}$$

This situation is graphically described in Figure 2 which shows the contribution to the total time-dependent $G_{22}(t)$ perturbation factor from probes that reach their final stable electronic configuration at a time t'. In this figure, $G_{22}(t)$ was

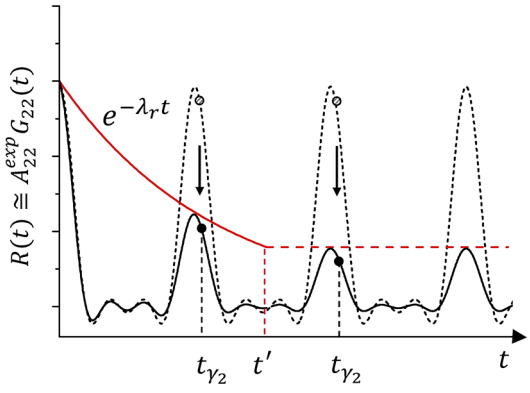

Figure 2. Graphical naive explanation of the construction of a contribution to the $R(t)$ spectrum corresponding to TDPAC probes (emitting γ_2 at different times t_{γ_2}) sensing a time-dependent *on−off* hyperfine interaction. $G_{22}(t)$ is the perturbation factor described in eq 7. Black dashed line: $R(t)$ spectrum for an axially symmetric static electric−quadrupole interaction (characterized by EFG1). Red solid line represents the pure dynamic interaction of eq 4, which is switched off after a time t' (red dashed line). Black solid line: contribution to the total time-dependent $R(t)$ spectrum from all the probes sensing a dynamic hyperfine interaction (with a final stable EFG1) as described by eq 7, reaching these probe atoms the same stable electronic configuration at a time t', emitting γ_2 at different times t_{γ_2}.

DOI: 10.1021/acs.jpcc.8b03724
J. Phys. Chem. C 2018, 122, 17423−17436

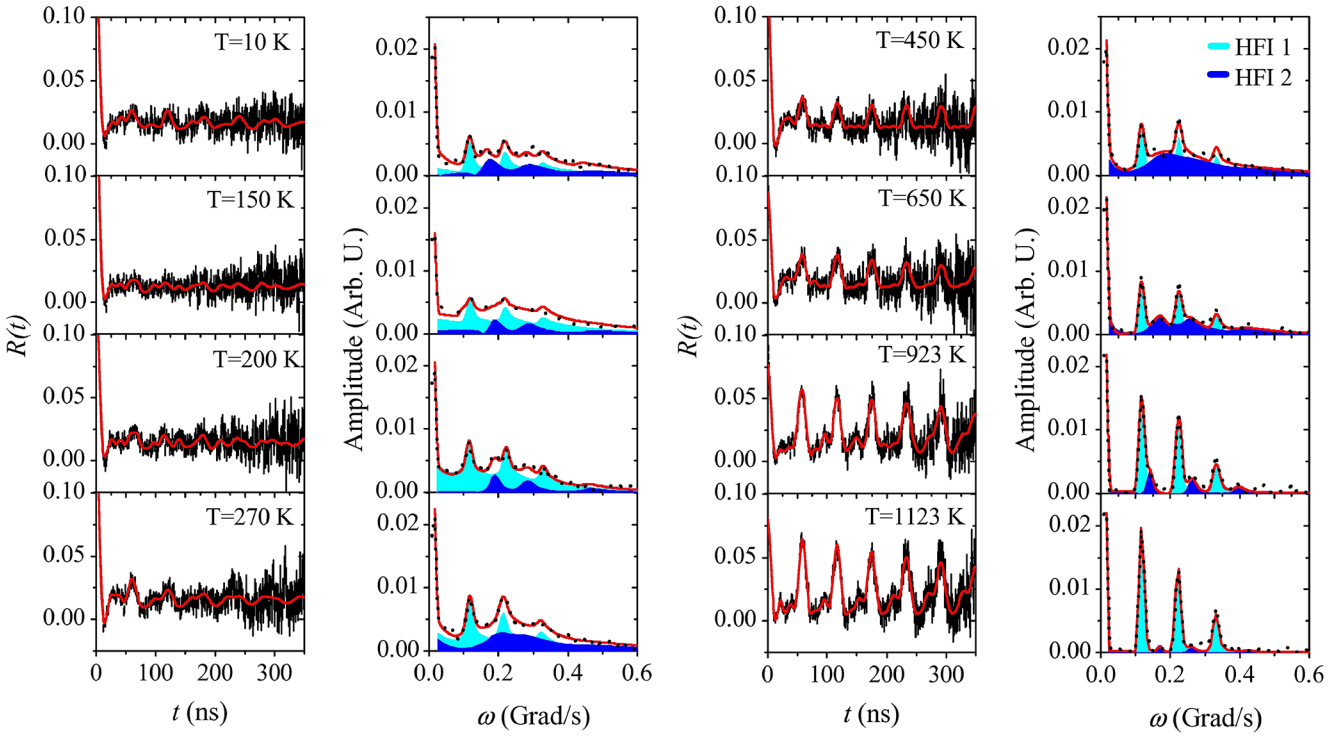

Figure 3. $R(t)$ spectra (left) and their corresponding Fourier transformed spectra (right) taken at the indicated selected measuring temperatures.

multiplied by the experimental anisotropy A_{22} to obtain this contribution to the $R(t)$ spectrum.

One way to obtain the total time-dependent perturbation factor $G_{22}(t)$ at a time t is to compute the average of eq 7, taken on the N atoms that emit γ_2 at time t, including those atoms that reach their final stable electronic state at time t' before t and those that are still excited at time t (i.e., t' is larger than t in eq 7):[36,45]

$$G_{22}(t) = N^{-1}\int_0^\infty G_{22}(t, t')P_g(t')\mathrm{d}t' \tag{8}$$

$$G_{22}(t) = N^{-1}\left(\int_0^t G^s_{22}(t)e^{-\lambda_r t'}\lambda_g N e^{-\lambda_g t'}\mathrm{d}t' + \int_t^\infty G^s_{22}(t)e^{-\lambda_r t}\lambda_g N e^{-\lambda_g t'}\mathrm{d}t'\right) \tag{9}$$

then

$$G_{22}(t) = \left[\frac{\lambda_r}{\lambda_r+\lambda_g}e^{-(\lambda_r+\lambda_g)t} + \frac{\lambda_g}{\lambda_r+\lambda_g}\right]G^s_{22}(t) \tag{10}$$

This model cannot be distinguished from the physically different case where there are *two fractions* of probes, f_d, undergoing a fluctuating field (without the *off* process) characterized by the perturbation factor

$$G_{22}(t) = G^s_{22}(t)e^{-\lambda t} \tag{11}$$

and f_s subjected only to the static field. Indeed, eq 10 is equivalent to

$$G_{22}(t) = [f_d e^{-\lambda t} + f_s]G^s_{22}(t) \tag{12}$$

if $f_d = \lambda_r/\lambda$, $f_s = \lambda_g/\lambda$, with $\lambda = \lambda_r + \lambda_g$. In eq 12, f_d, f_s, and λ are, in general, not correlated parameters. This is not the case, clearly, in the scenario represented by eq 10, which will be used to fit the $R(t)$ spectra.

In the case the probe atoms in a sample are localized at different environments, e.g., at nonequivalent cation sites of a crystal structure, eq 1 and eq 10 need to be modified accordingly using the usual model for multiple-site electric–quadrupole interactions for the static perturbation factor

$$R(t) \cong A_{22}^{\exp}G_{22}^{\exp}(t) = A_{22}^{\exp}\sum_i f_i G_{22_i}^{\exp}(t)$$

$$= A_{22}^{\exp}\sum_i f_i\left[\frac{\lambda_{r_i}}{\lambda_{r_i}+\lambda_{g_i}}e^{-(\lambda_{r_i}+\lambda_{g_i})t} + \frac{\lambda_{g_i}}{\lambda_{r_i}+\lambda_{g_i}}\right]G_{22_i}^{\exp}(t) \tag{13}$$

f_i being the fraction of nuclei that senses each time-dependent hyperfine interaction.

II.B. Sample Preparation and TDPAC Measurements.

The sample was prepared using high purity rutile SnO_2 powder (Sigma-Aldrich, purity better than 99.99%), pressed in a circular pellet of 5 mm diameter at 3×10^8 Pa, and annealed in air for 1 h at 423 K, plus 6 h at 773 K and 10 h at 1073 K in order to sinter and improve its crystallinity. The ^{111}In-($\rightarrow^{111}$Cd) isotope was introduced afterward by thermal diffusion, dropping approximately 10 μCi of $^{111}InCl_3$ dissolved previously in 0.05 normal HCl solution in water. This pellet was placed in a sealed quartz tube under N_2 atmosphere at low pressure (2×10^4 Pa) and annealed at 1073 K for 12 h.

The TDPAC spectrometer used was based on four BaF_2 scintillating detectors in a 90° coplanar arrangement and an electronic coincidence setup with slow–fast logic. The $R(t)$ spectrum was constructed for each measuring temperature, according to eq 1 from the 12 simultaneously recorded coincidence spectra, eight at 90° and four at 180°.

TDPAC measurements were carried out in the temperature range from 10 to 1123 K in a reversible way, in 50 or 25 K

DOI: 10.1021/acs.jpcc.8b03724
J. Phys. Chem. C 2018, 122, 17423−17436

steps. For measurements above RT, the sample was sealed in an evacuated quartz tube and performed in a small furnace with graphite electrodes positioned between detectors. For low-temperature measurements in the range from 10 to 295 K, the sample was attached to the coldfinger of a closed-cycle helium cryogenic device with temperature controlled to better than 0.1 K.

II.C. Experimental Results. In Figure 3 we show selected representative $R(t)$ spectra and their corresponding Fourier transformation measured at T = 10, 150, 200, 270, 450, 650, 923, and 1123 K. As is apparent, there is an increasing damping as measurement temperature decreases, starting from the very well-defined and undamped spectrum at T = 1123 K. This behavior is reversible with the measurement temperature.

Already at 1123 K two hyperfine interactions (corresponding to two different triplets of interaction frequencies) are resolved in the Fourier spectrum, although one of them (HFI1) accounts for almost 95% of the spectrum. Below 923 K a fast damping in the first ns of the $R(t)$ spectra is apparent but conserving this anisotropy for larger times. As mentioned before this effect increases as temperature decreases, in a reversible way. A good description of the $R(t)$ spectra with two pure static hyperfine interactions (using the perturbation factor of eq 3) was only possible for temperatures above 923 K. Hence, as explained in section II.A, the (red) solid lines in the $R(t)$ spectra of Figure 3 are the best least-squares fit of eq 13 to the experimental data. The (red) solid lines in the Fourier spectra are the Fourier transformation of the $R(t)$ fits.

Two hyperfine interactions (HFI1 and HFI2) were necessary to account for the $R(t)$ spectra along the entire temperature range of measurement. The contributions of HFI1 and HFI2 are shown as shaded areas (in light blue and blue, respectively) in the Fourier spectra (Figure 3). The fitted more relevant hyperfine parameters are shown in Figure 4 as a function of temperature. In this figure, the fitting errors on ω_Q and η are smaller than the data points. In the case of the fractions f, the errors are about ±5%, and errors in λ_r and λ_g are about 10% (not included in this figure for clarity). As mentioned in section II.A, the λ_r relaxation constant represents the damping strength in a pure time-dependent interaction (see eq 4) related with the transitions among different probe's charge states, λ_g being the inverse of the mean lifetime of the "electronic holes", τ_g, which governs the "on−off time" of the dynamic interaction. In addition, Figure 5 shows the relative weights of the *dynamic* and *static* terms of eq 12 for HFI1 and HFI2.

The combined inspection of the evolution of the hyperfine parameters (Figure 4), the dynamic and static fraction extracted from eq 12 (Figure 5), and the contributions of HFI1 and HFI2 to the Fourier spectra (Figure 3) enable us to describe the scenario sensed by the ^{111}Cd probe atoms as a function of temperature. Above 923 K the spectra present a pure static behavior, with more than 80% of probes sensing HFI1, characterized at T = 1123 K by ω_{Q_1} = 17.9(2) Mrad/s and η_1 =0.13(1), in agreement with the values of the single hyperfine interaction observed by Wolf et al.[24] While f_1 varies with temperature as seen in Figure 4a, ω_{Q_1} and η_1 are almost constant as well as its EFG distribution (δ_1 < 2%, with an incertitude of 10%). This constancy was also observed by Wolf et al.[24] The hyperfine parameters of HFI1 are also in agreement with the characterization performed at RT by Rentería et al.[27] in crystallized SnO_2 thin films and with one of

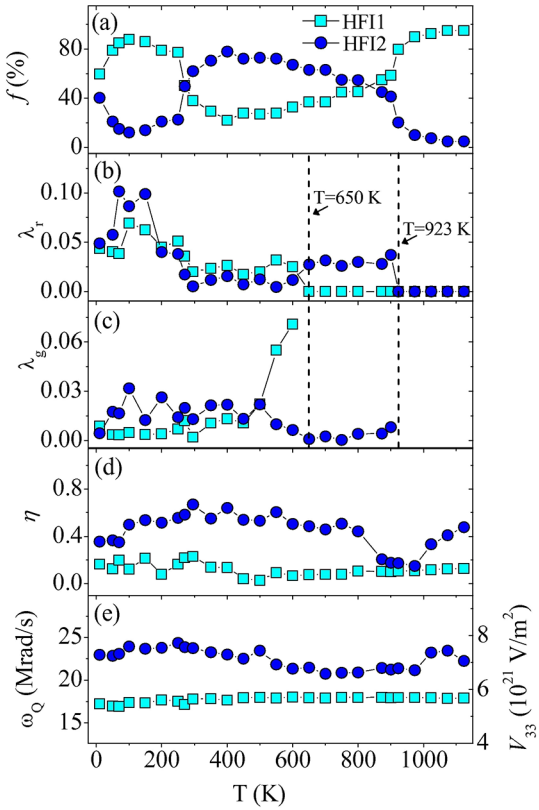

Figure 4. Evolution of (a) fractions and (b)−(e) hyperfine parameters λ_r, λ_g, η, and ω_Q (or V_{33}), of both hyperfine interactions HFI1 and HFI2, as a function of the measurement temperature T.

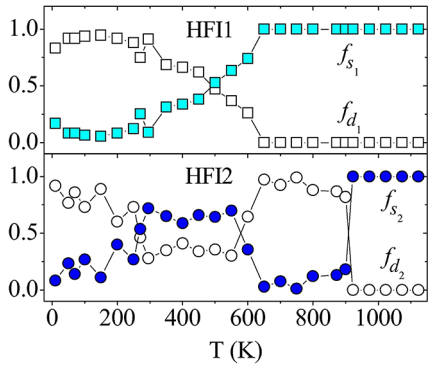

Figure 5. f_s and f_d for HFI1 (upper) and HFI2 (lower) hyperfine interactions, computed using eq 12 and the fitted λ_r and λ_g parameters shown in Figures 4b and 4c.

the hyperfine interactions reported by Ramos et al.[23] in ^{111}In-diffused SnO_2 nanopowders. As Figure 5 (upper) shows, f_s of HFI1 (solid light-blue squares) equals 100% from 1123 to 650 K and then decreases as T decreases with a step-like behavior. This is in agreement with the temperature behavior of the "static fraction" of the single hyperfine interaction reported by Wolf et al.[24] On the other hand, f_s of HFI2 is 100% only from 1123 to 923 K (see lower part of Figure 5). Between 923 and 650 K only HFI2 presents a dynamic behavior (see Figures 4b, 4c, and Figure 5 (lower)). As these figures show, neither of the interactions has a pure static behavior for T lower than 650 K. HFI2 is characterized along all the temperature range of measurement by ω_{Q_2} = 21−24 Mrad/s and η_2 = 0.2−0.6 (see Figures 4d and 4e), with an EFG distribution δ_2 of around 5%,

DOI: 10.1021/acs.jpcc.8b03724
J. Phys. Chem. C 2018, 122, 17423−17436

rising up to 20−30% for medium temperatures (270−550 K), with an incertitude of around 15%.

At this point, the results obtained applying the "on−off" B−O model for the $R(t)$ of eq 13 let us propose the following scenario for the ^{111}Cd probe atoms. At high T ($T \geq 923$ K), all the probes feel a pure static EFG, with more than 90% of them sensing an EFG reflecting the same final stable electronic state (EFG1) reached after the "*turn off*" of the dynamic process, a process that is observed for HFI1 only below 650 K. The rest of the probes (10%) sense a temperature-dependent EFG corresponding to different final stable charge states of the ^{111}Cd impurity (see ω_{Q_2} in Figure 4e), reached after the "*turn off*" of the dynamic process for each temperature (process only observed below 923 K in the case of HFI2). At medium and low T, the probe senses initially a *combined* static and time-dependent interaction (see eq 5) related with randomly fluctuating EFGs originated in the transitions between different electronic configurations of the probe atom (different charge states of ^{111}Cd including the corresponding final stable charge state related with EFG1 or EFG2, characterizing HFI1 or HFI2, respectively) until the "*turn off*" of this process. After this, the probe senses a pure static interaction (characterized by EFG1 or EFG2) related with the final stable electronic charge state the probe reaches at each temperature. It is useful to point out again that EFG1 is the same for all temperatures, while EFG2 is temperature dependent (see Figure 4e).

On the other hand, the fractions f_1 and f_2 of probes that feel the final EFG1 and EFG2, respectively, change with temperature (see Figure 4a). As T decreases, f_2 increases, and HFI2 begins to sense the dynamic interaction (below 923 K), while f_1 decreases, HFI1 being still a static interaction (only above 650 K). In view of the fact that f_1 increases with temperature and reaches more than 90% above 923 K, a temperature region with a larger electron availability due to thermal effects, and EFG1 being the same for all temperatures, it is reasonable to suppose that EFG1 is related with a probe's charge state with more electrons than those associated with EFG2.

In general, as T decreases, the electron availability and/or mobility could be decreasing in the system, as suggested by the increase of λ_r and the constancy of λ_g (i.e., with large values for τ_g) at low T (see Figures 4b and 4c). In effect, the increase of λ_r reflects an increase of the strength of the random fluctuation among different electronic configurations due to a decreasing electron availability, as T decreases. On the other hand, large τ_g values could be understood in terms of low electron availability and mobility. Following this idea, the fraction evolution of HF1 and HF2 from high temperature to RT could be explained by a decrease of the available electrons of the host; i.e., the relative lack of electrons as T decreases produces a decrease of the number of probes that senses EFG1 and an increase of those atoms that sense the interaction related with EFG2 (which need less electrons than EFG1, as we supposed above). At T lower than RT, f_1 unexpectedly increases again. However, at the same time both λ_{r_1} and λ_{r_2} strongly increase (especially λ_{r_2}), while τ_{g_1} and τ_{g_2} remain relatively constant at very large values (see Figures 4b and 4c). Both effects, more electronic holes with large lifetimes giving rise to both time-dependent interactions, produce the charge required to increase the fraction of probes that feel EFG1 as the final state.

Finally, based on the constancy of ω_{Q_1} and η_1 and the low value of δ_1 along the entire temperature range of measurement, their agreement with the values reported by Wolf et al. for the single interaction observed in their experiments, and the static character of the EFG1 along a wide high-temperature range, we tentatively assigned HFI1 to ^{111}Cd probes localized at cation sites of the SnO_2 crystalline structure. While HFI1 should be correlated with the same final charge state of the impurity, the oscillating behavior and large EFG2 distribution suggest that HFI2 should be correlated with slightly different final electronic configurations of ^{111}Cd also localized at Sn sites. In our scenario, as mentioned before, the probe's electronic configuration giving rise to EFG1 should have more electrons than the different configurations that produce the temperature-dependent values of EFG2. This assumption will be discussed in detail with the help of the ab initio study of the impurity−host system, described in what follows.

III. *AB INITIO* CALCULATIONS

III.A. Calculations Details. In order to enlighten the experimental TDPAC results described in the preceding section we performed electronic structure DFT-based *ab initio* calculations in Cd-doped rutile SnO_2. To simulate an isolated impurity, as is the case of ^{111}Cd atoms doped in our TDPAC samples with ppm impurity dilution, we used a supercell (SC) size so that each impurity does not interact with the nearest ones and that the structural relaxations of its neighbors do not affect the relaxations of other neighbors of the closest impurities. This SC ($2 \times 2 \times 3$ SC) is formed by 12 unit cells of rutile SnO_2. This unit cell is tetragonal with $a = b = 4.7374(1)$ Å and $c = 3.1864(1)$ Å,[52,53] and it contains two Sn atoms at positions $2a$ (0; 0; 0) and (1/2, 1/2, 1/2) and four O atoms at positions $4f$ $\pm(u, u, 0)$ and $\pm(1/2 + u, 1/2 - u, 1/2)$, with $u = 0.3056(1)$[52] or 0.3064(4).[53] In this structure, Sn has an octahedral oxygen coordination with four oxygen atoms (O2) forming the octahedron basal plane and two O1 atoms in the vertex of the octahedron (see Figure 6a). The resulting $2 \times 2 \times 3$ SC is tetragonal with lattice parameters $a' = 2a = b' = 2b = 9.47$ Å and $c' = 3c = 9.56$ Å, obtaining $c'/a' = 1.01$. In this SC, one of the 24 Sn atoms is replaced by a Cd one (Figure 6b), obtaining $Sn_{0.958}Cd_{0.042}O_2$, with the shortest distance between Cd impurities of about 9.5 Å. We studied the convergence of the structural relaxations and the hyperfine parameters in other SCs formed by $2 \times 2 \times 2$ and $2 \times 2 \times 4$ unit cells, checking that the $2 \times 2 \times 3$ SC was sufficient to simulate the isolated impurity, as usually occurs in oxides with an impurity−impurity shortest distance of around 10 Å.[13,15,18]

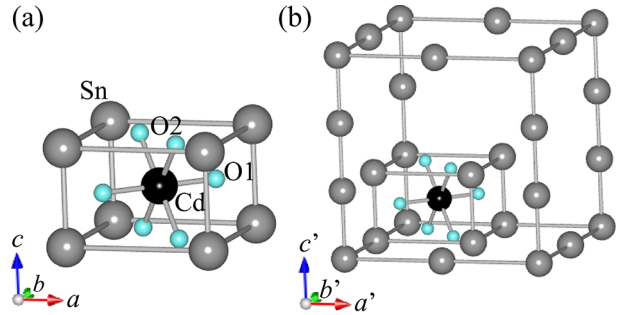

Figure 6. (a) Rutile SnO_2 unit cell. (b) Supercell with $a' = 2a$, $b' = 2b$, and $c' = 3c$. The gray, black, and light-blue spheres correspond to Sn, Cd, and O atoms, respectively.

In order to describe real samples, and particularly in our case where an electronic recombination process around the impurity occurs, it is essential to be able to predict with

DOI: 10.1021/acs.jpcc.8b03724
J. Phys. Chem. C 2018, 122, 17423−17436

accuracy the charge state of the impurity and therefore to describe correctly the structural, electronic, and hyperfine properties of the impurity−host system. In this sense, we performed calculations for different charge states of the impurity taking into account the nominal double acceptor character of Cd^{2+} when it replaces a Sn^{4+} in the SnO_2 host. For this, we add electrons to the SC (once a Sn atom is replaced by a Cd atom) in 0.1 e^- steps and up to 2 e^-, and we will call $SnO_2:Cd^{x-}$ the SC when x electrons are added to the SnO_2:Cd system.

The *ab initio* calculations have been performed employing the Full-Potential Augmented Plane Waves plus local orbitals (FP-APW+lo) method[54] embodied in the WIEN2k code.[55] The cutoff parameter of the plane wave bases in the interstitial region was $R_{MT}K_{max} = 7$, where K_{max} is the maximum modulus of the lattice vectors in the reciprocal space, and R_{MT} is the smallest radius of the nonoverlapping muffin-tin spheres centered in the atoms. In our calculations we use R_{MT}(Cd) = 1.06 Å, R_{MT}(Sn) = 0.95 Å, and R_{MT}(O) = 0.86 Å. In the reciprocal space, the integration was performed using the tetrahedron method,[56] taking 50 k-points in the first Brillouin zone. We checked that when using the reported values for $R_{MT}K_{max}$, R_{MT}, and k-points the EFG tensor and the total energy are converged for all the systems studied. Exchange and correlation effects were treated using the local-density approximation (LDA)[57] and the generalized gradient approximation (GGA). For GGA we used the Perdew−Burke−Ernzerhof (PBE-GGA) parametrization[58] and the GGA parametrization proposed by Wu and Cohen (WC-GGA).[59] In order to obtain the equilibrium structures of the SC, all atoms were displaced following a Newton dampened scheme[60] and repeating it until the forces on the ions were below 0.01 eV/Å. Finally, the EFG tensor was calculated from the second derivative of the obtained full electric potential.[61,62]

III.B. Calculation Results. *III.B.1. Structural Relaxation.* The substitution of a lattice native Sn atom by a Cd impurity induces considerable large forces acting on Cd and its neighboring atoms as well as, to a lesser extent, on the rest of the atoms of the SC. In the Cd-doped 2 × 2 × 3 SC, we checked if the final equilibrium positions obtained after the relaxation process depend on the initial structure (lattice and internal parameters) or not. We started the relaxation process using both the experimental and the *ab initio* optimized structural parameters of pure SnO_2 (extensively studied in ref 15), obtaining almost the same final structure. This can be explained by the enormous relaxation of Cd's nearest oxygen neighbor positions with respect to the subtle atomic position refinement obtained in the structural optimization process in pure SnO_2. What is relevant for our study is that the atomic equilibrium final positions of the neighboring atoms of Cd are the same, and hence the electronic configuration and the hyperfine properties at the Cd site do not depend on the initial positions used in the calculations.

In Table 1 we compare the Cd−O1 and Cd−O2 bond lengths, obtained after the equilibrium positions are achieved in $SnO_2:Cd^0$, $SnO_2:Cd^{1-}$, and $SnO_2:Cd^{2-}$, to the Sn−O1 and Sn−O2 bond lengths in pure SnO_2. As we see, the differences between the predicted Cd−O1 and Cd−O2 bond lengths using LDA, WC-GGA, and GGA approximations are less than 0.3%. For all charge states, the ONN (O1 and O2) atoms relax outward, enlarging the Cd−ONN distance. These dilatations are isotropic and depend strongly on the charge state of the impurity, increasing as electrons are added to the system. The magnitude and sense (outward or inward) of the bond-length relaxations introduced by the Cd impurity when it replaces a Sn atom are related with the difference between their ionic radii, that are 0.69 and 0.95 Å for 6-fold coordinated Sn^{4+} and Cd^{2+}, respectively.[63] In effect, in ref 15 it was shown that there exists a positive proportionality between the ONN bond-length relaxations and the ionic radii of Ta and Cd impurities relative to the radius of the native cation replaced by the impurities in rutile oxides. Moreover, the oxygen relaxations follow a general trend already observed in Cd-doped binary oxides with different crystal structures, in which the Cd impurity tries to reconstruct the Cd−ONN bond length of 2.35 Å that it has in its most stable oxide CdO.[64] The largest relaxations were found for the $SnO_2:Cd^{2-}$ SC due to the additional Coulomb repulsion originated when two electrons were added. Nevertheless, this relaxation does not reach the "ideal" value 2.35 Å that Cd has in CdO since the presence of the nearest Sn atoms of each ONN limits the Cd−ONN relaxation.

Table 1. Experimental Sn−O1 and Sn−O2 Bond Lengths for Pure SnO_2 (First Line) and Predicted Equilibrium Cd−O1 and Cd−O2 Distances for $SnO_2:Cd^0$, $SnO_2:Cd^{1-}$, and $SnO_2:Cd^{2-}$, Using the LDA, WC-GGA, and PBE-GGA Approximations

		dCd−O1 (Å)	dCd−O2 (Å)
SnO_2[a]		2.047	2.057
$SnO_2:Cd^0$	LDA	2.112	2.147
	WC-GGA	2.110	2.149
	PBE-GGA	2.110	2.151
$SnO_2:Cd^{1-}$	LDA	2.132	2.161
	WC-GGA	2.127	2.165
	PBE-GGA	2.126	2.168
$SnO_2:Cd^{2-}$	LDA	2.158	2.203
	WC-GGA	2.153	2.204
	PBE-GGA	2.152	2.207

[a]Ref 52.

III.B.2. Electronic Structure. In addition to the structural relaxations, the substitution of a Sn atom by a Cd impurity produces strong changes in the electronic structure of the semiconductor. Figures 7a and 7b show the density of electronic states (DOS) for pure SnO_2 and $SnO_2:Cd^0$, respectively, after the equilibrium atomic positions are reached. Comparing these DOS one can see that the Cd impurity introduces an acceptor impurity level at the top of the valence band (VB), basically formed by Cd-d and ONN-p states. These states contribute also to the bottom and the top of the VB, respectively. This situation is better shown in the atom-projected partial DOS (PDOS) of Figure 7c. On the right side of Figures 7b and 7c, magnifications of the DOS in the energy range of the acceptor impurity level are also shown. Integration of the empty states within the impurity level until the Fermi level (i.e., $E = 0$ eV) for the $SnO_2:Cd^0$ system (see right side of Figure 7b) gives a value of 2 e^-, confirming the double acceptor character of the Cd^{2+} impurity replacing a Sn^{4+} in SnO_2.

In Figure 8, the PDOS of Cd-d, O1-p, and O2-p for $SnO_2:Cd^0$, $SnO_2:Cd^{1-}$, and $SnO_2:Cd^{2-}$ are shown for the impurity level energy region. As we can see, when additional charge is added to the *neutral* system ($SnO_2:Cd^0$) up to 2 electrons, this charge goes to the Cd impurity and the ONN atoms, filling only states with symmetries d_{z^2}, $d_{x^2-y^2}$, and d_{xz} of

DOI: 10.1021/acs.jpcc.8b03724
J. Phys. Chem. C 2018, 122, 17423−17436

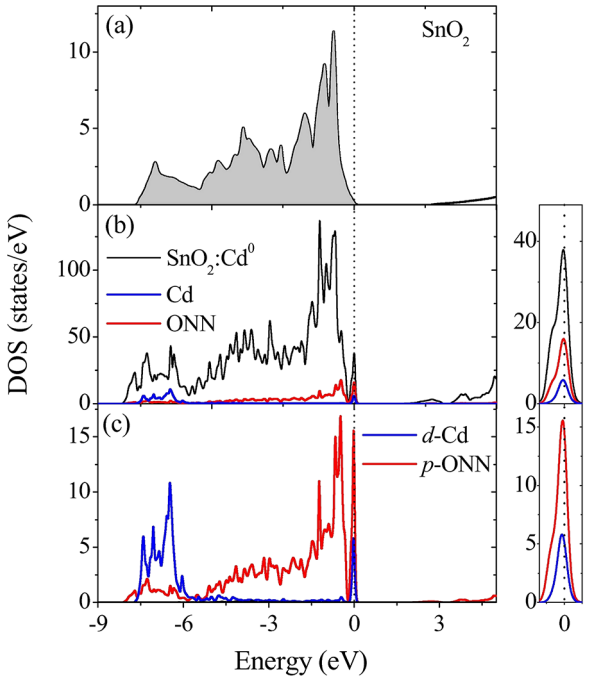

Figure 7. (a) Total density of states (DOS) for pure SnO_2. The shaded area shows the occupied states. (b) Total DOS (black) and atom-resolved partial DOS (PDOS) projected at Cd (blue) and ONN (red) sites for the SnO_2:Cd^0 system. (c) PDOS of d and p contributions at Cd and ONN sites, respectively. The energy is referred to as the last occupied state (vertical dotted line). On the right of (b) and (c) panels we show a zoom of the impurity level region.

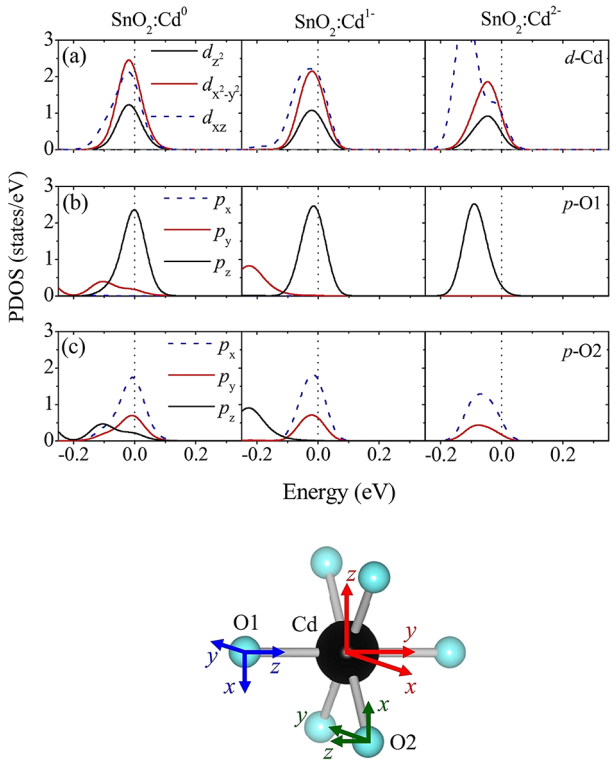

Figure 8. (a) PDOS of d contributions projected at the Cd site and (b) and (c) PDOS of p contributions projected at O1 and O2 sites, respectively, for SnO_2:Cd^0, SnO_2:Cd^{1-}, and SnO_2:Cd^{2-} systems. The energy is referred to the last occupied state (vertical dotted line). At the bottom are shown the local coordinate axes systems in which Cd-, O1-, and O2-projected PDOS were calculated.

Cd, p_z of O1, and p_x and p_y of the O2 atoms (see center and right columns in Figure 8), in agreement with the coordination geometry of the cationic site in the rutile structure. We have demonstrated that the added electrons are localized in the Cd−O1 and Cd−O2 bonds. In effect, the bottom part of Figure 8 shows the local coordinate systems used in the calculations in which the Cd-d and O-p orbitals are referred. According to this, O1-p_z orbitals point along the Cd−O1 bond and the hybridization of O2-p_x and O2-p_y orbitals along the Cd−O2 bonds, these bonds being shown in Figure 9. This figure shows the electron density, in the $(1\bar{1}0)$ and (110) lattice planes containing Cd and O1 and Cd and O2 atoms, respectively. Figures 9a and 9b correspond to the electron density for the first electron added to the SnO_2:Cd^0 system; Figures 9c and 9d correspond to the second electron added to the SnO_2:Cd^{1-} system; and Figures 9e and 9f correspond to the two electrons added to the SnO_2:Cd^0 system. To obtain the electron densities of Figure 9, the calculations were performed for selected occupied states in the impurity level energy region of the SnO_2:Cd^{1-} system for Figures 9a and 9b and the SnO_2:Cd^{2-} system for Figures 9c and 9d. In the case of Figures 9e and 9f we use the occupied states corresponding to the last two electrons below the Fermi energy in the SnO_2:Cd^{2-} system. Comparing Figures 9a and 9b, the first electron added to the SC has a preference to be localized at Cd and the O1 atoms along the Cd−O1 bonds, whereas the second electron added prefers to be localized at Cd and the O2 atoms along the Cd−O2 bonds. This is in part because once the first electron added, the Coulombian electronic repulsion with the second electron along the Cd−O1 axis is stronger. With respect to the *d*-charge which is localized at the Cd

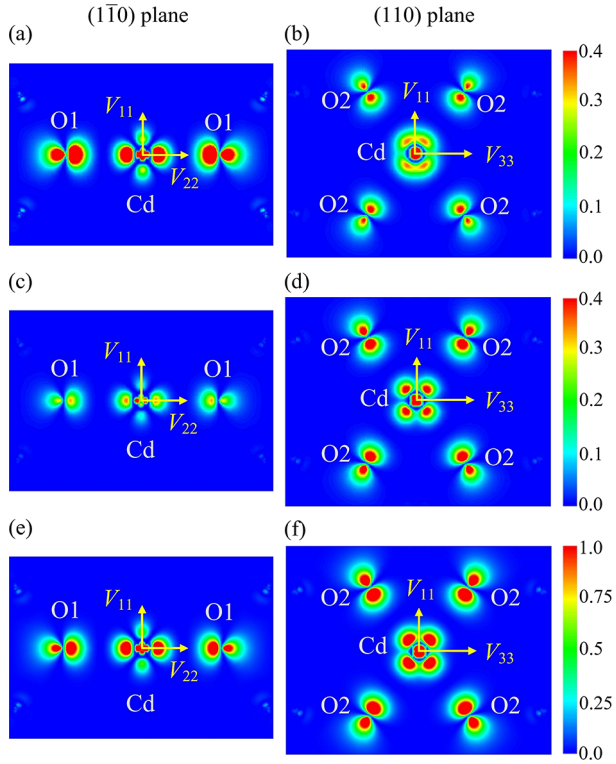

Figure 9. Electron density for (a) and (b) the first electron, (c) and (d) the second electron, and (e) and (f) the two electrons added to the SC, in the $(1\bar{1}0)$ (left column) and (110) (right column) planes.

DOI: 10.1021/acs.jpcc.8b03724
J. Phys. Chem. C 2018, 122, 17423−17436

impurity when one or two electrons are added to the system, the second bump of the radial wave function of the Cd orbitals in Figure 9 helps to identify the symmetries dominant in each plane. In Figure 9a Cd-d_{z^2} and $d_{x^2-y^2}$ orbitals are present, while the hybridization of Cd-d_{z^2} and $d_{x^2-y^2}$ can be detected in Figure 9b (depleted charge along the x axis), as well as an additional contribution of Cd-d_{xz} (see also the local coordinate axes systems at Cd shown in Figure 8). As mentioned before, the second electron has mainly Cd-d_{xz} character (see Figure 9d), while the hybridization of Cd-d_{z^2} and $d_{x^2-y^2}$ is more pronounced, as can be deduced from the depleted charge region along the x axis.

III.B.3. EFG. With the aim to explain the origin of the EFG tensors that characterize the two hyperfine interactions observed in the TDPAC experiments and the potential EFG dependence with the charge state of the impurity that could give account of the dynamic character of these interactions, we carried out EFG calculations at Cd sites in SnO_2 as a function of the impurity charge state. The EFG tensors calculated for the three charge states of the SCs SnO_2:Cd^0, SnO_2:Cd^{1-}, and SnO_2:Cd^{2-}, taking into account the full structural relaxation produced in each system, are quoted in Table 2.

Table 2. V_{33}, η, and V_{33} Direction Predicted for SnO_2:Cd^0, SnO_2:Cd^{1-}, and SnO_2:Cd^{2-} Using the LDA, WC-GGA, and PBE-GGA Approximations[a]

		V_{33} (10^{21} V/m^2)	η	V_{33} direction
SnO_2:Cd^0	LDA	+5.24	0.46	[1$\bar{1}$0]
	WC-GGA	+5.15	0.40	[1$\bar{1}$0]
	PBE-GGA	+5.11	0.36	[1$\bar{1}$0]
SnO_2:Cd^{1-}	LDA	+6.17	0.59	[1$\bar{1}$0]
	WC-GGA	+5.97	0.52	[1$\bar{1}$0]
	PBE-GGA	+5.91	0.50	[1$\bar{1}$0]
SnO_2:Cd^{2-}	LDA	+5.43	0.14	[1$\bar{1}$0]
	WC-GGA	+5.67	0.20	[1$\bar{1}$0]
	PBE-GGA	+5.75	0.19	[1$\bar{1}$0]
Exp. HFI1		5.68(1)	0.13(1)	-----

[a]The experimental values of HFI1 are shown for comparison.

Little differences exist between V_{33} and η predicted by LDA, WC-GGA, and PBE-GGA approximations. These differences are due to the small difference in the final equilibrium positions predicted by each approximation (see Table 1), due to the strong r^{-3} EFG dependence from the charge sources. Due to this r^{-3} dependence, the EFG at the Cd site is basically originated in the nonspherical electronic charge density very close to the Cd nucleus (in the first bump of the Cd's radial wave functions).[62] It is important to notice here that, as occurred in many other doped binary oxide systems,[15,18,65,66] these approximations predict the same EFG tensor (within the precision of the calculations) when the same structural positions are employed. The V_{33} direction is parallel to the [1$\bar{1}$0] crystal axis (see Figures 6 and 9) for all these charge states and is the same that it has in pure SnO_2 and Ta-doped SnO_2 at Sn and Ta sites, respectively.[15] While V_{33} slightly increases and decreases when 1 and 2 electrons are added to the SC, respectively, the η parameter that describes the symmetry of the charge density around the probe nucleus changes drastically once the second electron is added. In order to understand this drastic change and the unexpected V_{33} slight variation, we performed a systematic calculation of the EFG varying, between 0 and 2 electrons, ad the negative charge added to the *neutral* SC, in steps of 0.1 e^-. Figure 10 shows the result of these calculations for the LDA approximation. In it,

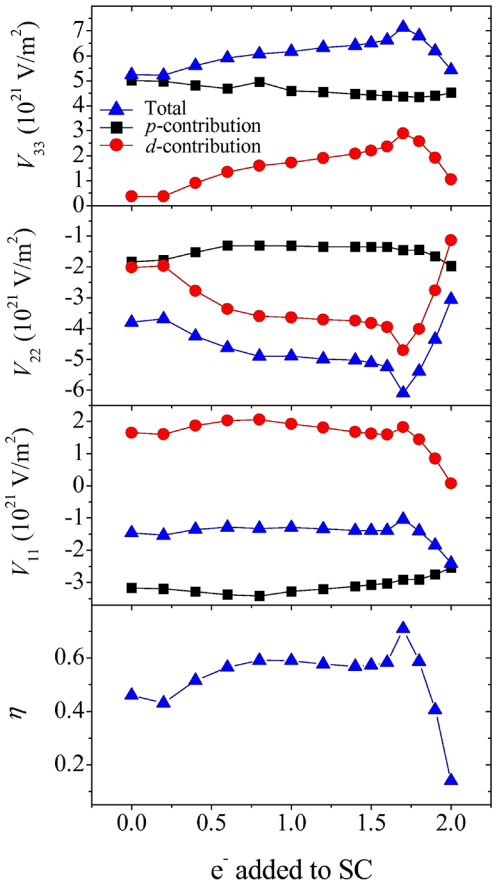

Figure 10. V_{33}, V_{22}, V_{11}, and η parameter (blue triangles) as a function of the number of electrons added to the SC. For each V_{ii}, the p and d contributions (black squares and red circles, respectively) are shown.

the asymmetry parameter and the p and d contributions to the total V_{ii} principal components of the EFG are plotted as a function of the added charge. This study enables the detection of an increase in V_{33} and η as electrons are added to the SC and an abrupt decrease of their values for the charge states close to the complete ionization of the impurity level, i.e., when this level is almost filled. While the p contribution to V_{ii} is almost constant for different charge states (and dominant for V_{33} as already observed in other Cd-doped binary oxides),[13,67] the d contribution changes strongly, leading to the shape of the total V_{ii} dependence with the impurity charge state. The strong decrease of η toward an axially symmetric situation (η = 0.14) is explained by the strong variation of V_{11} and V_{22}, governed again by the variation of the d contribution. In effect, V_{11} and V_{22} are almost equal when 2 electrons are added to the SC, leading to η close to zero.

The constancy of the p contribution to V_{ii} as a function of the impurity charge state (from 0 to 2 electrons) can now be understood by the fact that the p-states of Cd are almost only present in the VB, whereas the d-states are present both in the VB and in the impurity level. Considering, roughly speaking, that the VB states do not change when the impurity level is being filled (*rigid-band* model), the behavior of the EFG should be described by the change of the relative occupation of Cd-d orbitals with $d_{x^2-y^2}$, d_{xz}, and d_{z^2} symmetries. A closer

DOI: 10.1021/acs.jpcc.8b03724
J. Phys. Chem. C 2018, 122, 17423−17436

inspection of the electronic densities in the neighborhood of the Cd nucleus plotted at selected planes containing Cd and its ONN (see Figure 9), which corresponds directly to the above-mentioned Cd-d orbital symmetries within the acceptor impurity level, could explain the behavior of the EFG as a function of the impurity charge state (Figure 10). For this description, we will take into account that a negative point charge along a certain axis produces a negative EFG component in this direction, while if this charge is localized in a plane normal to this direction it produces a positive EFG component with half of the precedent value. In general, the sign and strength of the EFG component along a certain axis originated by a negative charge q situated at an angle Φ from this axis is given by

$$V_{ii}(\vec{r}) = \frac{q(3\cos^2\Phi - 1)}{4\pi\varepsilon_0 r^3} \quad (14)$$

Hence, negative point charges localized between 0° and 54.7° from a certain principal i axis produce a negative V_{ii} value.

In effect, as described in detail in the previous section, the addition of one electron to the SnO_2:Cd^0 SC produces a much larger localization of electronic charge along the Cd−O1 bonds than the charge added along the Cd−O2 bonds. Hence, as mentioned above, the addition of this negative charge along the V_{22} direction produces a positive increase in V_{33}, since the V_{33} direction is normal to V_{22}. This effect continues increasing V_{33} up to its maximum value and then abruptly decreases when the acceptor impurity level is completely filled. In effect, the second added electron goes mainly to the Cd−O2 bonds (see Figures 9c and 9d), producing an electronic configuration in which the relative amount of charge along V_{22} is smaller with respect to the charge distributed in the x−z plane (see the local coordinate axes system at Cd in Figure 8, at the bottom). This charge, which corresponds mainly to Cd-d_{xz} orbitals, is close to 45° from the V_{33} axis (see Figure 9d), producing a negative contribution to V_{33} (according to eq 14), hence decreasing the positive V_{33} value (see Figure 10, first panel).

Following the same ideas, the addition of the first electron along mainly the V_{22} direction increases the negative V_{22} value (from −2 to -5×10^{21} V/m^2, see Figure 10), and the addition of the second electron decreases this negative value (from −5 to −1) since the additional charge in the x−z plane normal to V_{22} originates a positive EFG contribution to V_{22}. In the same way, the addition of the second electron that goes mainly to the x−z plane contributes with a negative EFG along the z axis, decreasing the V_{11} positive value (see Figure 10, 3rd panel).

IV. COMPARISON BETWEEN EXPERIMENTAL TDPAC RESULTS AND THE *AB INITIO* CALCULATIONS

Even though there was a seeming constancy of V_{33} for the three different charge states of the impurity quoted in Table 2, the strong V_{ii} variation as a function of the Cd charge state (displayed in Figure 10), in particular near the completely ionized double acceptor state, justifies the existence of the randomly fluctuating EFGs mentioned in the proposed B−O model described in section II.A. On the other hand, the comparison between the predicted results quoted in Table 2 and Figure 10 with the experimental EFG1 shows a perfect agreement only for the SnO_2:Cd^{2-} system. This let us to definitively assign HFI1 to completely ionized ^{111}Cd probes localized at defect-free substitutional Sn sites.

The mean values of V_{33} and η of HFI2 (see Figures 4d and 4e) are in good agreement with the predicted EFGs obtained when 1.5 up to 1.9 electrons are added to the SnO_2:Cd^0 SC. In particular, the decrease of η_2 just above 800 K is compatible with a charge state of 1.9 electrons added to the SC. In the proposed scenario, for T above 923 K the number of electrons required by ^{111}Cd probes sensing HFI1 increases (due to the increase of f_1 as T increases above 923 K), and hence the number of available electrons filling holes at ^{111}Cd atoms that sense HFI2 decreases (leading to a charge state of ^{111}Cd, e.g., in the range of 1.5−1.8 added electrons), increasing η_2 again as T increases. Again, the agreement between experiment and the *ab initio* calculations let us to assign HFI2 to ^{111}Cd probes, localized at defect-free substitutional Sn sites, with final stable charge states close to the completely ionized state of the acceptor impurity level.

Finally, taking into account the V_{ii} behavior as a function of the charge state of the impurity and the proposed scenario within the B−O modelization, we showed that a slight variation of the Cd charge state when it traps between 1.5 to 2 electrons is enough to give rise to the hyperfine interactions (i.e., EFG1 and EFG2 tensors) observed in the TDPAC experiments.

V. SUMMARY AND CONCLUSIONS

TDPAC experiments were performed on high purity rutile SnO_2 polycrystalline samples using ^{111}Cd isotope as a probe atom as a function of measuring temperature in the range 10−1123 K in a reversible way. To introduce the radioactive ^{111}Cd impurities in the samples, its parent ^{111}In ($\rightarrow^{111}$Cd) was diffused under a nonoxidant N_2 atmosphere, aiming to substitute Sn atoms of the host lattice.

The TDPAC spectra showed a peculiar and increasing (reversible) damping as measuring temperature decreases that could be analyzed by a time-dependent perturbation factor in the framework of the Bäverstam and Othaz "on−off" model. Two hyperfine interactions, HFI1 and HFI2, were necessary to account for the spectra along the entire temperature range of measurement. Both interactions are static at high temperatures and time dependent at lower temperatures but below a different temperature threshold for each interaction. The time-dependent perturbation factor results, in the B−O model, in a combination of a *dynamic* and a *static* term. While HFI1 is purely static for $T \geq 650$ K, HFI2 is static only for $T \geq 923$ K. HFI1, characterized by EFG1, is very well-defined (monochromatic), with its hyperfine parameters independent of temperature. HFI2, characterized by EFG2, presents a much larger EFG (static) distribution, V_{33} and η being oscillating parameters around a mean value larger than those of HFI1. With respect to the parameters that characterize the dynamic behavior, the relaxation constant λ_r, which measures the attenuation strength originated in the fluctuating EFGs, increases for both interactions as T decreases. This can be explained in terms of an increasing number of electronic holes as T decreases due to the decrease of the electron availability related with the thermal ionization of defects. The lifetime of the electronic holes ($1/\lambda_g$) increases as T decreases in the case of HFI1 and has a rather constant large value in the case of HFI2. In our scenario, the large value of τ_g(HFI2) is due to the lack of enough electrons to fill the double acceptor level of the fraction of ^{111}Cd atoms that feel HFI2. On the other hand, the behavior of τ_g(HFI1) can be explained as follows: just above 650 K, τ_g is extremely short since there are enough number of

DOI: 10.1021/acs.jpcc.8b03724
J. Phys. Chem. C 2018, 122, 17423−17436

electrons available to rapidly ionize the small number of highly diluted ^{111}Cd atoms that feel HFI1 at this temperature. As T decreases, τ_g increases due to the loss of thermal-excited electrons that could completely ionize the acceptor level.

In the B−O model applied to interpret our experimental results, EFG1 and EFG2 are related with different final stable electronic configurations of the ^{111}Cd atom once the dynamic hyperfine interactions are *turned off*. The dynamic regime sensed by the ^{111}Cd nucleus is originated in the random fast fluctuations between different electronic configurations of the ^{111}Cd atom before arriving to the stable configurations that give rise to EFG1 and EFG2. Those configurations are correlated to different fluctuating charge states of the impurity (including those corresponding to the final stable configurations).

The detailed first-principles study of the electronic structure of Cd-doped SnO_2 showed that the Cd impurity introduces a double acceptor level in the top of the valence band and produces isotropic outward relaxations of the nearest oxygen neighbors that have to be taken into account self-consistently in order to correctly predict the hyperfine properties at the Cd site. The acceptor level has mainly contributions from Cd-d and ONN-p orbitals. In effect, when two electrons are added to the *neutral* Cd-doped SnO_2 SC, the acceptor level became completely filled, and hence this electronic charge contributes to enhance the electron density almost only at Cd and its ONN atoms. While the strength of V_{33} is mainly due to the Cd-p contribution (which is practically constant for the three V_{ii} components) present along all the valence band, its variation and that of the asymmetry parameter η as a function of the charge state of the impurity are due to the strong variation of the Cd-d contribution to V_{ii}, which in turn is related to the filling of the acceptor level, obtained adding from 0 to 2 electrons to the SC. This strong variation of the EFG was explained in terms of the variation in the occupancy of the Cd-d orbitals present in the acceptor level and the change in the anisotropy of the electronic density at the closest neighborhood of the Cd nucleus related with these orbitals.

The comparison between the *ab initio* predictions and the experimental EFG results enabled us to assign HFI1 to ^{111}Cd probes localized at defect-free cation sites of the rutile structure with a double acceptor level completely filled above T = 650 K. Below this temperature, these probe nuclei feel a dynamic hyperfine interaction whose final stable electronic configuration is that corresponding to the static EFG1 sensed above T = 650 K. This EFG1 is in perfect agreement with the EFG that characterizes the single hyperfine interaction observed by Wolf et al.,[24] with the high-temperature interaction found by Bibiloni et al.,[25] and with the interaction assigned to ^{111}Cd at Sn sites of the high-temperature crystalline phase in SnO_2 thin films.[27] On the other hand, HFI2 was assigned to ^{111}Cd probes localized at defect-free Sn sites with the double acceptor level partially filled (between 1.5 and 1.8 added electrons) above T = 923 K (static regime). Below this temperature, these probe nuclei feel a dynamic hyperfine interaction whose final stable configuration (depending on T) is one corresponding to the impurity level charge states with 1.5 to 1.8 added electrons.

The dynamic behavior of HFI1 (at lower T) and the existence of an unexpected second HFI2 (in a host with a single cation site such as SnO_2) assigned to ^{111}Cd probes that do not reach the complete ionization of the impurity acceptor state suggest that the parameters that characterize and give rise to the dynamic interactions depend on the insulating or semiconducting character of the host and hence on the electronic availability and mobility and, necessarily, on the variation of the EFG as a function of the charge state of the ^{111}Cd impurity. The variation of the EFG in turn depends on the adopted configuration of the Cd orbitals upon electron feeling (i.e., the resulting electronic density closest to the Cd nucleus) in each impurity−host system.

At this point we can conclude that the EC as well as the double acceptor character of the ^{111}Cd impurity contribute to the existence of the dynamic hyperfine interactions since they promote the presence of electronic holes localized at the ^{111}Cd atom with a lifetime long enough to be experimentally detected, depending on the conducting nature of the host. The same conclusion could be applied to ^{111}In(→Cd)-doped In-, Y-, and Sc-sesquioxides[44,68,69] in which dynamic hyperfine interactions were also observed, ^{111}Cd being a single acceptor in these hosts. To our knowledge, the ECAE seems to be a necessary condition to the observation of this type of time-dependent interaction in oxides, taking into account two facts: first, that up to now no time-dependent interactions like those described here have been observed in PAC experiments using ^{181}Hf(→^{181}Ta) in oxides, a probe that does not decay through EC; and second, when ^{111m}Cd(→^{111}Cd) was used in PAC experiments in some of the same oxides mentioned above, dynamic hyperfine interactions were not observed, or its effect was very weak.[51,70,71] At present, it is too early to confirm that the electronic acceptor character of the Cd probe atom is a necessary condition to observe dynamic interactions. For this, investigations in other binary oxides in which Cd would be an isovalent or a donor impurity in the host system should be performed. PAC experiments as well as *ab initio* calculations in this sense are currently in progress.

AUTHOR INFORMATION

Corresponding Authors

*E-mail: darriba@fisica.unlp.edu.ar.
*E-mail: renteria@fisica.unlp.edu.ar.

ORCID

Artur W. Carbonari: 0000-0002-4499-5949
Mario Rentería: 0000-0003-1396-4792

Notes

The authors declare no competing financial interest.

ACKNOWLEDGMENTS

This work was partially supported by Consejo Nacional de Investigaciones Científicas y Técnicas (CONICET, under Grants No. PIP0002 and PIP0803), Conselho Nacional de Desenvolvimento Científico e Tecnológico (CNPq, grant no. 305046/2013-6), and Fundação de Amparo a Pesquisa do Estado de São Paulo (FAPESP, grant no. 2014/14001-1). This research made use of the computational facilities of the Physics of Impurities in Condensed Matter (PhI) group at IFLP and Departamento de Física (UNLP). Prof. Dr. A.F. Pasquevich is gratefully acknowledged for very fruitful discussions about the time-dependent perturbation factor and the ECAE phenomena. The implementation of the time-dependent perturbation factor into the fitting program by Prof. Dr. A. Ayala is greatly acknowledged. E.L.M. wishes to thank the personnel at IPEN for their kind hospitality during his research stay. M.R. and G.N.D. are members of CONICET, Argentina.

DOI: 10.1021/acs.jpcc.8b03724
J. Phys. Chem. C 2018, 122, 17423−17436

REFERENCES

(1) Frank, G.; Kauer, E.; Kostlin, H.; Schmitte, F. J. Transparent Heat-Reflecting Coatings for Solar Applications Based on Highly Doped Tin Oxide and Indium Oxide. *Sol. Energy Mater.* **1983**, *8*, 387−398.

(2) Dawar, A. L.; Joshi, J. C. Semiconducting Transparent Thin Films: Their Properties and Applications. *J. Mater. Sci.* **1984**, *19*, 1−23.

(3) Korotcenkov, G.; Brinzari, V.; Boris, Y.; Ivanov, M.; Schwank, J.; Morante, J. Influence of Surface Pd Doping on Gas Sensing Characteristics of SnO_2 Thin Films Deposited by Spray Pirolysis. *Thin Solid Films* **2003**, *436*, 119−126.

(4) Wang, Y.; Wu, X.; Li, Y.; Zhou, Z. Mesostructured SnO_2 as Sensing Material for Gas Sensors. *Solid-State Electron.* **2004**, *48*, 627−632.

(5) Lee, J. Effects of Oxygen Concentration on the Properties of Sputtered SnO_2:Sb Films Deposited at Low Temperature. *Thin Solid Films* **2008**, *516*, 1386−1390.

(6) Toyosaki, H.; Kawasaki, M.; Tokura, Y. Electrical Properties of Ta-Doped SnO_2 Thin Films Epitaxially Grown on TiO_2 Substrate. *Appl. Phys. Lett.* **2008**, *93*, 132109.

(7) Nakao, S.; Yamada, N.; Hitosugi, T.; Hirose, Y.; Shimada, T.; Hasegawa, T. Fabrication of Highly Conductive Ta-doped SnO_2 Polycrystalline Films on Glass Using Seed-Layer Technique by Pulse Laser Deposition. *Thin Solid Films* **2010**, *518*, 3093−3096.

(8) Muto, Y.; Nakatomi, S.; Oka, N.; Iwabuchi, Y.; Kotsubo, H.; Shigesato, Y. High-Rate Deposition of Ta-doped SnO_2 Films by Reactive Magnetron Sputtering Using a Sn-Ta Metal-Sintered Target. *Thin Solid Films* **2012**, *520*, 3746−3750.

(9) Sun, P.; Zhou, X.; Wang, C.; Wang, B.; Xu, X.; Lu, G. One-Step Synthesis and Gas Sensing Properties of Hierarchical Cd-Doped SnO_2 Nanostructures. *Sens. Actuators, B* **2014**, *190*, 32−39.

(10) Mir, F. A.; Batoo, K. M.; Chatterjee, I.; Bhat, G. M. Preparation and AC Electrical Characterizations of Cd Doped SnO_2 Nanoparticles. *J. Mater. Sci.: Mater. Electron.* **2014**, *25*, 1564−1570.

(11) Mariappan, R.; Ponnuswamy, V.; Suresh, P.; Suresh, R.; Ragavendar, M.; Sankar, C. Deposition and Characterization of Pure and Cd doped SnO_2 Thin Films by the Nebulizer Spray Pyrolysis (NSP) Technique. *Mater. Sci. Semicond. Process.* **2013**, *16*, 825−832.

(12) Mishra, S. N.; Rots, M.; Cottenier, S. Dynamic Lattice Distortions in Sr_2RuO_4: Microscopic Studies by Perturbed Angular Correlation Spectroscopy and Ab Initio Calculations. *J. Phys.: Condens. Matter* **2010**, *22*, 385602.

(13) Darriba, G. N.; Rentería, M.; Petrilli, H. M.; Assali, L. V. C. Site Localization of Cd Impurities in Sapphire. *Phys. Rev. B: Condens. Matter Mater. Phys.* **2012**, *86*, 075203.

(14) Richard, D.; Muñoz, E. L.; Rentería, M.; Errico, L. A.; Svane, A.; Christensen, N. E. Ab Initio LSDA and LSDA+U Study of Pure and Cd-Doped Cubic Lanthanide Sesquioxides. *Phys. Rev. B: Condens. Matter Mater. Phys.* **2013**, *88*, 165206.

(15) Darriba, G. N.; Muñoz, E. L.; Errico, L. A.; Rentería, M. Ab Initio Study of Structural, Electronic and Hyperfine Properties of *n*-type SnO_2:Ta Semiconductor. *J. Phys. Chem. C* **2014**, *118*, 19929−19939.

(16) do Nascimento, R. R.; Lima, F. C. D. A.; Gonçalves, M. B.; Errico, L. A.; Rentería, M.; Petrilli, H. M. Metal Coordination Study at Ag and Cd Sites in Crown Thioether Complexes Through DFT Calculations and Hyperfine Parameters. *J. Mol. Model.* **2015**, *21*, 97.

(17) Alonso, R. E.; Errico, L. A.; Taylor, M.; Svane, A.; Christensen, N. E. Structural, Electronic and Hyperfine Characterization of Pure and Ta-Doped $ZrSiO_4$. *Phys. Rev. B: Condens. Matter Mater. Phys.* **2015**, *91*, 085129.

(18) Richard, D.; Darriba, G. N.; Muñoz, E. L.; Errico, L. A.; Eversheim, P. D.; Rentería, M. Experimental and First-Principles Theoretical Study of Structural and Electronic Properties in Tantalum-Doped In_2O_3 Semiconductor: Finding a Definitive Hyperfine Interaction Assignment. *J. Phys. Chem. C* **2016**, *120*, 5640−5650.

(19) Errico, L. A.; Lejaeghere, K.; Runco, J.; Mishra, S. N.; Rentería, M.; Cottenier, S. Precision of Electric-Field Gradient Predictions by Density Functional Theory and Implications for the Nuclear Quadrupole Moment and Its Error Bar of the ^{111}Cd 245 keV 5/2+ Level. *J. Phys. Chem. C* **2016**, *120*, 23111−120.

(20) Schell, J.; Lupascu, D. C.; Carbonari, A. W.; Mansano, R. D.; Freitas, R. S.; Gonçalves, J. N.; Dang, T. T.; Vianden, R. Cd and In-Doping in Thin Film SnO_2. *J. Appl. Phys.* **2017**, *121*, 195303.

(21) Moreno, M. S.; Desimoni, J.; Requejo, F. G.; Rentería, M.; Bibiloni, A. G.; Freitag, K. TDPAC Characterization of Tin Oxides Using ^{181}Ta. *Hyperfine Interact.* **1990**, *62*, 353−358.

(22) Moreno, M. S.; Desimoni, J.; Bibiloni, A. G.; Rentería, M.; Massolo, C. P.; Freitag, K. Crystallization Study and Hyperfine Characterization of a Sn-O Thin Film With ^{181}Ta. *Phys. Rev. B: Condens. Matter Mater. Phys.* **1991**, *43*, 10086−10092.

(23) Marques Ramos, J. M.; Martucci, T.; Carbonari, A. W.; de Souza Costa, M.; Saxena, R. N.; Vianden, R. Electric Field Gradient in Nanostructured SnO_2 Studied by Means of PAC Spectroscopy Using ^{111}Cd or ^{181}Ta as Probe Nuclei. *Hyperfine Interact.* **2013**, *221*, 129−136.

(24) Wolf, H.; Deubler, S.; Forkel, D.; Foettinger, H.; Iwatschenko-Borho, M.; Meyer, M.; Renn, M.; Witthuhn, W. Acceptors and Donors in the Wide-Gap Semiconductors ZnO and SnO_2. *Mater. Sci. Forum* **1986**, *10−12*, 863−868.

(25) Bibiloni, A. G.; Desimoni, J.; Massolo, C. P.; Rentería, M. Hyperfine Interaction Between Indium Atoms and Oxygen Vacancies in Stanic Oxide. *Phys. Rev. B: Condens. Matter Mater. Phys.* **1988**, *38*, 20−25.

(26) Moreno, M. S.; Bibiloni, A. G.; Massolo, C. P.; Desimoni, J.; Rentería, M. Search for Aftereffects in Tin Oxide Films. *Phys. Rev. B: Condens. Matter Mater. Phys.* **1989**, *40*, 2546−2548.

(27) Rentería, M.; Bibiloni, A. G.; Moreno, M. S.; Desimoni, J.; Mercader, R. C.; Bartos, A.; Uhrmacher, M.; Lieb, K. P. Hyperfine Interactions of ^{111}In-Implanted in Tin Oxide Thin Films. *J. Phys.: Condens. Matter* **1991**, *3*, 3625−3634.

(28) Ramos, J. M.; Carbonari, A. W.; Costa, M. S.; Saxena, R. N. Electric Quadrupole Interactions in Nano-Structured SnO_2 as Measured with PAC Spectroscopy. *Hyperfine Interact.* **2010**, *197*, 239−243.

(29) Bibiloni, A. G.; Desimoni, J.; Massolo, C. P.; Mendoza-Zélis, L.; Pasquevich, A. F.; Sánchez, F. H.; López-García, A. Temperature Dependence of Electron-Capture Aftereffects in the Semiconductor In_2O_3. *Phys. Rev. B: Condens. Matter Mater. Phys.* **1984**, *29*, 1109−1111.

(30) Bibiloni, A. G.; Massolo, C. P.; Desimoni, J.; Mendoza-Zélis, L. A.; Sánchez, F. H.; Pasquevich, A. F.; Damonte, L.; López-García, A. R. Time-Differential Perturbed-Angular-Correlation Study of Pure and Sn-Doped In_2O_3 Semiconductors. *Phys. Rev. B: Condens. Matter Mater. Phys.* **1985**, *32*, 2393−2400.

(31) Massolo, C. P.; Desimoni, J.; Bibiloni, A. G.; Mendoza-Zélis, L. A.; Damonte, L. C.; Lopez-García, A. R.; Martin, P. W.; Dong, S. R.; Hooley, J. G. Aftereffect Investigations in Mixed-Valence Indium Chlorides. *Phys. Rev. B: Condens. Matter Mater. Phys.* **1986**, *34*, 8857−8862.

(32) Frauenfelder, H.; Steffen, R. M. *Alpha-, Beta-, and Gamma-Ray Spectroscopy*; Vol. 2, Ed. by Seigbahn, K. North-Holland Publishing Co., Amsterdam, 1968.

(33) Kaufmann, E. N.; Vianden, R. J. The Electric Field Gradient in Noncubic Metals. *Rev. Mod. Phys.* **1979**, *51*, 161−214.

(34) Schatz, G.; Weidinger, A. *Nuclear Condensed Matter Physics: Nuclear Methods and Applications*; Wiley, Chichester, England, 1996.

(35) Rentería, M.; Requejo, F. G.; Bibiloni, A. G.; Pasquevich, A. F.; Shitu, J.; Freitag, K. Perturbed-Angular-Correlation Study of the Electric-Field Gradient in ^{181}Hf-Doped and Implanted Indium Sesquioxide. *Phys. Rev. B: Condens. Matter Mater. Phys.* **1997**, *55*, 14200−14207.

(36) Bäverstam, U.; Othaz, R.; De Sousa, N.; Ringström, B. After-Effects in the Decay of ^{57}As and ^{197m}Hg. *Nucl. Phys. A* **1972**, *186*, 500−512.

(37) Abragam, A.; Pound, R. V. Influence of Electric and Magnetic Fields on Angular Correlations. *Phys. Rev.* **1953**, *92*, 943−962.

DOI: 10.1021/acs.jpcc.8b03724
J. Phys. Chem. C 2018, 122, 17423−17436

(38) Lohstroh, A.; Uhrmacher, M.; Wilbrandt, P. J.; Wulff, H.; Ziegeler, L.; Lieb, K. P. Electronic Relaxation in Indium Oxide Films Studied with Perturbed Angular Correlations. *Hyperfine Interact.* **2004**, *159*, 35−42.
(39) Penner, J.; Vianden, R. Temperature Dependence of the Quadrupole Interaction for ^{111}In in Sapphire. *Hyperfine Interact.* **2004**, *158*, 389−395.
(40) Lupascu, D.; Habenicht, S.; Lieb, K. P.; Neubauer, M.; Uhrmacher, M.; Wenzel, T. Relaxation of Electronic Defects in Pure and Doped La_2O_3 Observed by Perturbed Angular Correlations. *Phys. Rev. B: Condens. Matter Mater. Phys.* **1996**, *54*, 871−883.
(41) Pasquevich, A. F.; Uhrmacher, M.; Ziegeler, L.; Lieb, K. P. Hyperfine Interactions of ^{111}Cd in Ga_2O_3. *Phys. Rev. B: Condens. Matter Mater. Phys.* **1993**, *48*, 10052−10062.
(42) Pasquevich, A. F. Preferential Site Occupation of Indium in β-Ga_2O_3. *Hyperfine Interact.* **1990**, *60*, 791−794.
(43) Muñoz, E. L.; Carbonari, A. W.; Errico, L. A.; Bibiloni, A. G.; Petrilli, H. M.; Rentería, M. TDPAC Study of Cd-Doped SnO. *Hyperfine Interact.* **2007**, *178*, 37−43.
(44) Bartos, A.; Lieb, K. P.; Pasquevich, A. F.; Uhrmacher, M. ISOLDE collaboration. Scaling of the Electric Field Gradient of ^{111}Cd Impurities in the Bixbyite Oxides of Y, Sc, Dy and Yb. *Phys. Lett. A* **1991**, *157*, 513−518.
(45) Pasquevich, A. F.; Rentería, M. Impurity Centers in Oxides Investigated by γ-γ Perturbed Angular Correlation Spectroscopy and *Ab Initio* Calculations. *Defect Diffus. Forum* **2011**, *311*, 62−104.
(46) Sato, W.; Itsuki, Y.; Morimoto, S.; Susuki, H.; Nasu, S.; Shinohara, A.; Ohkubo, Y. Local Fields and Conduction-Electron Behavior at Impurity Sites in Indium-doped ZnO. *Phys. Rev. B: Condens. Matter Mater. Phys.* **2008**, *78*, 045319.
(47) Muñoz, E. L. Estudio Experimental y de Primeros Principios de Interacciones Hiperfinas Dinámicas en Óxidos Semiconductores Dopados con Impurezas (^{111}In(EC)→)^{111}Cd. Ph.D. Thesis, Universidad Nacional de La Plata, La Plata, Argentina, March 2011. http://sedici.unlp.edu.ar/handle/10915/2628 (accessed June 6, 2018).
(48) Dang, T. T.; Schell, J.; Lupascu, D. C.; Vianden, R. Dinamic Quadrupole Interactions in Semiconductors. *J. Appl. Phys.* **2018**, *123*, 165109.
(49) Mendoza-Zélis, L. A.; Bibiloni, A. G.; Caracoche, M. C.; López-García, A. R.; Martínez, J. A.; Mercader, R. C.; Pasquevich, A. F. Temperature Dependence of the Electric Field Gradient at Ta Nuclei in Hafnium Pyrovanadate. *Hyperfine Interact.* **1977**, *3*, 315−320.
(50) Dillenburg, D.; Maris, Th. A The Effect of Statistical Perturbations on Angular Correlations. *Nucl. Phys.* **1962**, *33*, 208−217.
(51) Habenicht, S.; Lupascu, D.; Uhrmacher, M.; Ziegeler, L.; Lieb, K. P. PAC-Studies of Sn-Doped In_2O_3: Electronic Defect Relaxation Following the ^{111}In(EC)^{111}Cd-Decay. *Z. Phys. B: Condens. Matter* **1996**, *101*, 187−196.
(52) Bolzan, A. A.; Fong, C.; Kennedy, B. J.; Howard, C. J. Structural Studies of Rutile-Type Metal Dioxides. *Acta Crystallogr., Sect. B: Struct. Sci.* **1997**, *53*, 373−380.
(53) Hazen, R. M.; Finger, L. W. Bulk Moduli and High-Pressure Crystal Structures of Rutile-Type Compounds. *J. Phys. Chem. Solids* **1981**, *42*, 143−151.
(54) Madsen, G. K. H.; Blaha, P.; Schwarz, K.; Sjöstedt, E.; Nordström, L. Efficient linearization of the Augmented Plane-Wave Method. *Phys. Rev. B: Condens. Matter Mater. Phys.* **2001**, *64*, 195134.
(55) Blaha, P.; Schwarz, K.; Madsen, G.; Kvasnicka, D.; Luitz, J. *WIEN2k, An Augmented Plane Wave + Local Orbitals Program for Calculating Crystal Properties*; Technical Universität Wien, Austria, 2012.
(56) Blöchl, P. E.; Jepsen, O.; Andersen, O. K. Improved Tetrahedron Method for Brillouin-Zone Integrations. *Phys. Rev. B: Condens. Matter Mater. Phys.* **1994**, *49*, 16223−16233.
(57) Perdew, J. P.; Wang, Y. Accurate and Simple Analytic Representation of the Electron-Gas Correlation Energy. *Phys. Rev. B: Condens. Matter Mater. Phys.* **1992**, *45*, 13244−13249.
(58) Perdew, J. P.; Burke, K.; Ernzerhof, M. Generalized Gradient Approximation Made Simple. *Phys. Rev. Lett.* **1996**, *77*, 3865−3868.
(59) Wu, Z.; Cohen, R. E. More Accurate Generalized Gradient Approximation for Solids. *Phys. Rev. B: Condens. Matter Mater. Phys.* **2006**, *73*, 235116.
(60) Kohler, B.; Wilke, S.; Scheffler, M.; Kouba, R.; Ambrosch-Draxl, C. Force Calculation and Atomic-Structure Optimization for the Full-Potential Linearized Augmented Plane-Wave Code WIEN. *Comput. Phys. Commun.* **1996**, *94*, 31−48.
(61) Schwarz, K.; Ambrosch-Draxl, C.; Blaha, P. Charge Distribution and Electric-Field Gradients in $YBa_2Cu_3O_{7-x}$. *Phys. Rev. B: Condens. Matter Mater. Phys.* **1990**, *42*, 2051−2061.
(62) Blaha, P.; Schwarz, K.; Dederichs, P. H. First-Principles Calculation of the Electric-Field Gradient in hcp Metals. *Phys. Rev. B: Condens. Matter Mater. Phys.* **1988**, *37*, 2792−2796.
(63) Shannon, R. D. Revised Effective Ionic Radii and Systematic Studies of Interatomic Distances in Halides and Chaleogenides. *Acta Crystallogr., Sect. A: Cryst. Phys., Diffr., Theor. Gen. Crystallogr.* **1976**, *32*, 751−767.
(64) Wyckoff, R. W. G. *Crystal Stuctures*; Wiley: New York, USA, 1964; Page 16, Vol. *II*.
(65) Errico, L. A.; Rentería, M.; Petrilli, H. M. Cd in SnO: Probing Structural Effects on the Electronic Structure of Doped Oxide Semiconductors Through the Electric Field Gradient at the Cd Nucleus. *Phys. Rev. B: Condens. Matter Mater. Phys.* **2007**, *75*, 155209.
(66) Darriba, G. N.; Errico, L. A.; Eversheim, P. D.; Fabricius, G.; Rentería, M. First-Principles and Time-Differential γ-γ Perturbed-Angular-Correlation Spectroscopy Study of Structural and Electronic Properties of Ta-Doped TiO_2 Semiconductor. *Phys. Rev. B: Condens. Matter Mater. Phys.* **2009**, *79*, 115213.
(67) Errico, L. A.; Fabricius, G.; Rentería, M. Metal Impurities in an Oxide: *Ab Initio* Study of Electronic and Structural Properties of Cd in Rutile TiO_2. *Phys. Rev. B: Condens. Matter Mater. Phys.* **2003**, *67*, 144104.
(68) Bolse, W.; Uhrmacher, M.; Kesten, K. The EFG of the In-O-Bond In_2O_3, AgO and Ag_2O. *Hyperfine Interact.* **1987**, *35*, 931−934.
(69) Muñoz, E. L.; Richard, D.; Carbonari, A. W.; Errico, L. A.; Rentería, M. PAC Study of Dynamic Hyperfine Interactions at ^{111}In-doped Sc_2O_3 Semiconductor and Comparison with *Ab Initio* Calculations. *Hyperfine Interact.* **2010**, *197*, 199−205.
(70) Uhrmacher, M. Application of Perturbed Angular Correlations to Oxides. *Phys. B* **2007**, *389*, 58−66.
(71) Habenicht, S.; Lupascu, D.; Neubauer, M.; Uhrmacher, M.; Lieb, K. P. ISOLDE-Collaboration. Doping of Sapphire Single Crystals with 111In and 111Cd Detected by Perturbed Angular Correlation. *Hyperfine Interact.* **1999**, *120/121*, 445−448.

DOI: 10.1021/acs.jpcc.8b03724
J. Phys. Chem. C 2018, 122, 17423−17436